

# A three-dimensional numerical approach on water entry of a horizontal circular cylinder using the volume of fluid technique

A. Iranmanesh, M. Passandideh-Fard\*

Mechanical Engineering Department, Ferdowsi University of Mashhad, Mashhad, Iran

## ARTICLE INFO

### Keywords:

Water entry  
Volume of fluid (VOF)  
Horizontal circular cylinder  
Free-surface flows

## ABSTRACT

In this paper, complicated hydrodynamics of a horizontal circular cylinder entering water is investigated numerically for low Froude numbers. A numerical approach is used to model the solid-liquid interactions in presence of a free-surface. The governing equations for the 3D incompressible fluid flow are continuity and Navier-Stokes equations along with an equation for the free surface advection. To track the free-surface motion, the fast-fictitious-domain method is integrated into the volume-of-fluid (VOF) technique. The governing equations are solved everywhere in the computational domain including the horizontal cylinder. A rigid body motion is applied to the region occupied by the circular cylinder. The no-slip boundary condition on the solid-liquid interface is exerted implicitly via increasing the viscosity of the region occupied by the solid. To validate the numerical scheme, the results are compared with those of the experiments available in the literature. The effects of cylinder diameter, length, impact velocity, and cylinder-water density ratio on the non-dimensional depth are also investigated.

## 1. Introduction

Water entry problems have been studied theoretically and experimentally by many researchers and scientists for more than a century due to their extensive applications in numerous industries especially ocean and coastal engineering. Some water entry applications are namely: hydrodynamic loading on ships, ship slamming, launching of torpedoes, sea-landing of aerial vehicles, missile projectiles' impact upon entering water, and even steel-making processes. However, cavity formation behind the solid object and capillary effects at the contact line between the surface of the solid and liquid complicates the understanding and analysis of this phenomenon.

Worthington and Cole (1897) presented an initial image of water impact cavity and splash by using single-spark photography. Water entry of vertical spherical objects was studied systematically by Worthington (1908). The solid-liquid interaction knowledge was improved comprehensively by later studies. Watanabe (1934) performed a quantitative experimental work to measure the impact force on an object upon entering water. The effect of various surface conditions of a sphere on the cavity formed during its water entry was investigated by May (1951). He also conducted (May, 1952) many experiments to analyze the effect of various parameters on the cavity which formed behind the solid. The effect of atmospheric pressure, solid velocity, and surface tension on the entry of spheres into water was studied by

Gilberg and Andersok (1948). It was concluded that the closure of splash was mostly dependent on an increase in atmospheric density and solid velocity. They also found that the splash closure was influenced by surface tension only in cases where the solid radius, velocity, and the atmospheric density are small. Several experiments were performed by Abelson (1970) to investigate pressure drop behind a solid object moving inside a liquid. The initial force of the impact on a sphere striking a liquid surface was estimated experimentally by Moghisi and Squire (1981). They also improved the correlation for the drag coefficient of a sphere during its initial entry into a liquid. Greenhow and Lin (1983) presented typical images for the free surface deformation during the water entry of two-dimensional cylinders. They assumed the length of the cylinder to be nearly the same as that of the tank to create a two-dimensional cavity following the cylinder impact. A whole cavity evolution for a horizontal cylinder was not created in their experiments since the depth of water was supposed to be shallow. Hu and Koterayama (1996) experimentally and numerically investigated the hydrodynamic forces acting on a rectangular cylinder and a circular cylinder undergoing slow drift oscillation in regular waves. The viscous flow around a two-dimensional oscillating cylinder was modelled using a finite-difference method. Lee et al. (1997) considered the effect of Bernoulli pressure and surface tension on the splash closure. They found that both inertia and gravity effects are relevant to the deep closure for water entry with low Froude numbers. Thoroddsen et al.

\* Corresponding author.

E-mail addresses: [iranmanesh.aghil@gmail.com](mailto:iranmanesh.aghil@gmail.com) (A. Iranmanesh), [mpfard@um.ac.ir](mailto:mpfard@um.ac.ir) (M. Passandideh-Fard).

(2004) worked on the horizontal jetting ejected from the impact point of a sphere with a high velocity at the initial stage. It was found that this initial axisymmetric jetting spreads radially outwards at a speed of up to 30 times of the sphere velocity. They also concluded that the initial jetting forms within mostly 100  $\mu$ s from the first contact of the sphere on water. Experimental-theoretical studies for water entry of hydrophobic spheres and vertical cylinders were presented by Aristoff and Bush (2009) and Aristoff et al. (2010). A regime diagram for hydrophobic spheres with the same wetting properties based on non-dimensional parameters affecting the cavity formation behind the sphere were also presented. A theoretical model for predicting key parameters namely the depth and time of pinch-off, depth of sphere at the pinch-off time and volume of cavity behind the sphere were also developed.

A new Lagrange-multiplier based on the fictitious-domain method for the direct numerical simulation of fluid-solid interaction was proposed by Glowinski et al. (1999). They also utilized this multiplier for fluidization, sedimentation, and many other applications (Glowinski et al., 1999, 2001; Glowinski, 2003). The fast computation scheme proposed by Patankar (2001) was used by Patankar and Sharma (2005) to simulate rigid particulate flows. In this method, computation domain included both solid and liquid and the governing equations were solved everywhere. The solid velocity was calculated by integrating in the solid zones since the total linear and angular moment in each individual solid zone was supposed to be conserved. Zhu et al. (2006) numerically analyzed the water entry and exit of a horizontal circular cylinder with both forced and free vertical motions using the Constrained Interpolation Profile (CIP) method. The governing equations were solved numerically on a non-uniform, staggered Cartesian grid. The numerical results of the free-surface deformation, the vertical motion of the cylinder as well as the water entry and exit forces were compared with the experimental results. Hu and Sueyoshi (2010) introduced two numerical approaches namely the CIP-based Cartesian grid method and the MPS method to simulate the strongly nonlinear wave-body interaction problems such as ship motions and green-water impact on deck. The numerical results were validated with experimental data for a dam break problem. An experimental investigation of the trajectories, forces, and cavity formation behind spinning hydrophobic and hydrophilic spheres were presented by Techet and Truscott (2011). Several cases were presented for non-spinning spheres including half hydrophobic and half hydrophilic. They concluded that the spin induced less lateral forces compared to asymmetrical cavity formation. Mirzaii and Passandideh-Fard (2012) developed a 2D numerical algorithm for simulating the interactions between a liquid and a solid object in presence of a free-surface. The fast-fictitious-domain method was integrated into the volume of fluid (VOF) technique to track the free surface motion. The model was also used to simulate the free fall of one and two circular particles inside a liquid. Two-dimensional numerical simulations of the water entry and exit of horizontal circular cylinders at a constant velocity were described by Hafsia et al. (2009). The simulated results were compared with the numerical results of Lin (2007). The free surface deformation around the cylinder in the downward direction was accurately predicted. A proposed experimental setup for characterizing the vertical motion of a horizontal circular cylinder through a free surface was presented by Goharzadeh and Molki (2012). Their experimental results gave insight on hydrodynamic impact phenomena and surface waves. Yang and Qiu (2012a, 2012b) investigated 3D slamming problems for water entry of solid bodies with vertical and oblique velocities using the CIP method. A pressure-based algorithm was introduced for non-advection calculations while the advection terms were modelled by the 3D CIP method. They also calculated hydrodynamic forces on a wedge, a cusped body, and a sphere and compared the numerical results with those of the experiments. Yang and Qiu (2012a, 2012b) calculated slamming forces on 2D and 3D bodies using the CIP method. The advection terms were calculated using a compact upwind scheme while the multiple phases

were simulated by a pressure-based algorithm. 2D wedges with deadrise angles varying between 0 and 60° were considered to validate the numerical scheme. Their 2D model was extended to 3D and was applied for simulating a cylinder and a catamaran entering calm water. Lue et al. (2012) studied experimentally and numerically the slamming load and response of complex steel wedge with a deadrise angle of 22°. They measured impact acceleration, slamming pressure, and stress responses and compared the results with those of the simulations. They found that the numerical model well predicted the stress trends and its maximum. Ryzhakov et al. (2013) investigated the behavior of the sea-landing of an unmanned aerial vehicle using the Particle Finite Element Method. They reported the maximum load exerted upon the floats to vary between 4 and 6 kN depending on water accumulation in the vehicle. Three assumptions of water accumulation (front, rear, lateral) were also considered. They found the vehicle to be stable and floatable in all scenarios. Larsen (2013) studied the possibility of water entry problems using the CD-adapco CFD-software STAR-CCM+ with a focus on circular cylinders. Two scenarios were considered, a cylinder with a constant velocity and a free-falling cylinder. He also compared the numerical results of three-dimensional water impact of a cylinder with 8° impact angle with those of experiments and a good agreement was observed. Gu et al. (2014) simulated water entry of solid objects with various shapes and configurations by applying the Navier-Stokes equations on a fixed Cartesian grid. The level set method was used to capture the free surface deformation. Moving objects were modelled using the partial cell method combined with a local relative velocity approach. They modelled vertical and oblique water entry of wedges with different heel angles and compared the results with those of the simulations available in the literature. Wang and Soares (2014) studied the water impact of three-dimensional buoys by an explicit finite element method with an Arbitrary-Lagrangian Eulerian solver. The fluid-solid interface was modelled using the VOF method. The convergence studies were achieved for three dimensional hemisphere and cones with various deadrise angles. The numerical results were found to be highly influenced by the domain mesh size. Abraham et al. (2014) numerically evaluated the forces and motions of a sphere falling on a water surface from an elevation above the free-surface. They concluded that the drag force was highly dependent on the momentum transfer from the sphere to the adjacent liquid. Three-dimensional effects on water entry of the horizontal cylinders were investigated by Wei and Hu (2014). They examined four length to diameter ratios, two cylinder-water density ratios, and two falling heights in their experiments. The effect of diameter on the cylinder depth, however, was not considered. They concluded that the measured jetting speeds for all studied cases were approximately equal at the initial stage since the kinetic energy of the flow was nearly two-dimensional. A numerical study on the dynamic response of a generic rigid water-landing object during water impact was presented by Challa et al. (2014). They validated the numerical results with those of the experiments. They investigated a wide range of conditions considering variations in vertical velocity, entry angle, and object weight. The numerical results showed that the first coupled Fluid-Structure Interaction (FSI) model could capture the water-impact response accurately for all range of drop tests considered. A detailed study on the local pressures acting on the surface of a quasi-rigid cylinder during vertical water entry into a flat water surface was accomplished by Nuffel et al. (2014). Their works encompassed the impact pressure results of a large set of slamming drop experiment with a cylindrical model. They found that for deadrise angles larger than 4.25°, the Wagner theory (Wagner, 1932) was a good approximation for impact pressures acting on a horizontal rigid cylinder during vertical water entry. A series of experimental studies on water entry of circular cylinders with inclined angles was presented by Wei and Hu (2015). They focused on the effect of inclined angles as well as density and length-to-diameter ratios. Both quantitative and qualitative analyses were carried out based on the experimental results. They reported that the cylinder with a lower inclined angle experienced a larger drag

force. Pancioli et al. (2015) performed several experiments on water entry of curved rigid wedges with deadrise angles of 25° and 35° as well as varying radius of curvature. They varied the drop height to study the effects of the impact velocity on the pile-up evolution, the impact dynamics, and the energy transferred to the fluid. It was found that between 60% and 80% of the impact energy was transferred to the risen water which formed the pile-up and the spray jets. Erfanian et al. (2015) studied experimentally and numerically the water entry of a spherical-nose projectile. A Coupled Eulerian-Lagrangian method was used to model the fluid-structure interaction. They compared the cavity shape and the projectile trajectory of the numerical results with those of the experiments where good agreement was observed. Wen and Qiu (2016) simulated two-dimensional water entry of a wedge, a ship section, and a circular cylinder using the CIP method. They defined density functions to capture the interface between solid, water, and air.

In this paper, a three-dimensional numerical approach is developed to obtain the cavity formed behind a horizontal circular cylinder impacting a free surface. The continuity and Navier-Stokes equations are solved simultaneously along with the VOF method to track the free-surface. The solid body motion is generated by applying the conservation of momentum within the solid to the region occupied by the cylinder. The numerical results are validated with experimental results both quantitatively and qualitatively. Furthermore, the effects of length, diameter, cylinder-water density ratio, and impact velocity on the cylinder motion are also investigated.

## 2. Numerical method

### 2.1. Fluid flow

The continuity and Navier-Stokes equations in 3D, incompressible, Newtonian, and laminar flow are solved as the governing equations for fluid flow:

$$\nabla \cdot \vec{V} = 0 \tag{1}$$

$$\frac{\partial \vec{V}}{\partial t} + \vec{V} \cdot \nabla \vec{V} = -\frac{1}{\rho} \nabla p + \frac{1}{\rho} \nabla \cdot \vec{\tau} + \frac{1}{\rho} \vec{F}_b \tag{2}$$

$$\vec{\tau} = \mu[(\nabla \vec{V}) + (\nabla \vec{V})^T] \tag{3}$$

where  $\vec{V}$  is the velocity vector,  $\rho$  the density,  $\mu$  the dynamic viscosity,  $p$  the pressure,  $\vec{\tau}$  the stress tensor, and  $\vec{F}_b$  stands for body forces per unit volume acting on the fluid. It should be mentioned that for all cases considered in this study, the maximum Reynolds number for a horizontal circular cylinder entering water is  $3.09 \times 10^5$ ; therefore, the flow can be assumed laminar.

A two-step projection method (Passandideh-Fard et al., 2002) is used to solve the continuity and momentum equations in two fractional steps. In the first step,  $\vec{V}^{\rightarrow n+1/2}$  is obtained by discretizing the convective and body force terms explicitly.

$$\frac{\vec{V}^{\rightarrow n+1/2} - \vec{V}^{\rightarrow n}}{\Delta t} = -(\vec{V} \cdot \nabla \vec{V})^n + \frac{1}{\rho^n} \nabla \cdot \mu[(\nabla \vec{V})^n + (\nabla \vec{V})^n]^T + \frac{1}{\rho^n} \vec{F}_b \tag{4}$$

In Eq. (4), superscript (n) specifies the quantity magnitude at the old time level and  $\Delta t$  is the time step size. By employing explicit discretization for viscous terms, a first temporary velocity is calculated.

Finally, the following equation must be solved to obtain velocity vector at the new time level ( $\vec{V}^{\rightarrow n+1}$ ).

$$\frac{\vec{V}^{\rightarrow n+1} - \vec{V}^{\rightarrow n+1/2}}{\Delta t} = -\frac{1}{\rho^n} \nabla p^{n+1} \tag{5}$$

If divergence operator is applied to right and left sides of Eq. (5)

and the continuity equation is used, the pressure Poisson equation will be obtained as following:

$$\nabla \cdot \left[ \frac{1}{\rho^n} \nabla p^{n+1} \right] = \frac{\nabla \cdot \vec{V}^{\rightarrow n+1/2}}{\Delta t} \tag{6}$$

Incomplete Cholesky-Conjugate Gradient (ICCG) solver (Kershaw, 1978) is selected to solve the resulting equation by which the pressure is obtained. This pressure is next used to calculate the final velocity at the next time level (n+1) using Eq. (5).

To track the interface, the VOF method is used where a scalar field (f), the so-called liquid volume fraction, is defined:

$$f = \begin{cases} 0 & \text{in gas or solid} \\ 0 < f < 1 & \text{at liquid interface} \\ 1 & \text{inside liquid} \end{cases} \tag{7}$$

It should be noted that f is defined as the fraction of total volume of a cell occupied by liquid. Therefore, f is the volume of liquid in a cell divided by the total volume of the cell (not divided by the combined volume of liquid and gas).

Once the new velocity field is computed, values of f are obtained by solving an advection equation for volume fraction:

$$\frac{df}{dt} = \frac{\partial f}{\partial t} + \vec{V} \cdot \nabla f = S \tag{8}$$

where S represents the mass transfer term which is supposed to be zero in this study. Eq. (8) is solved based on the Youngs PLIC algorithm to track the interface (Youngs, 1984).

Landau and Lifschitz (1987) suggested the following boundary condition at the moving liquid/gas interface:

$$(p_l - p_g - \sigma \kappa) n_i = (\tau_{l,ik} - \tau_{g,ik}) n_k + \frac{\partial \sigma}{\partial x_i} \tag{9}$$

The pressures on the liquid and gas sides of the interface are defined by  $p_l$  and  $p_g$ , respectively. A component of the unit normal  $\hat{n}$  directed into the interface is represented by  $n_i$ ;  $\sigma$  stands for the surface tension;  $\kappa$  is the local total curvature; and  $\tau_{l,ik}$  and  $\tau_{g,ik}$  are shear stresses in liquid and gas, respectively. To simplify the above-mentioned equation, the surface tension is supposed to be constant while the shear stresses are assumed zero to satisfy the interface boundary condition. Thus, Eq. (9) is reduced to Laplace equation as following:

$$p_l - p_g = \sigma \kappa \tag{10}$$

Instead of using Eq. (10) as a boundary condition for the pressure field, the surface tension is reformulated as a body force ( $F^{ST}$ ) based on the Continuum Surface Force (CSF) model proposed by Brackbill et al. (1992). The following equation is suggested by Aleinov and Puckett (1995):

$$\vec{F}^{ST} = \sigma \kappa \frac{A}{V} \hat{n} \tag{11}$$

where V is the cell volume and A is the surface area of the fluid contained within the cell.  $\kappa$  and  $\hat{n}$  are calculated using the following relations:

$$\kappa = -\nabla \cdot \hat{n} \tag{12}$$

$$\hat{n} = \frac{\nabla f}{|\nabla f|} \tag{13}$$

The body force calculated from this methodology is substituted into Eq. (4) to consider the effect of surface tension.

### 2.2. Solid object

The fast-fictitious-domain method is used to model the solid object. To satisfy the no-slip boundary condition on the solid-liquid interface,

a high viscosity is attributed to the solid zone. As the first step for this method, the governing equations are solved everywhere including the solid object without any further considerations. As the second step, the rigid body motion of the solid object can be imposed based on the fact that the total angular and linear momentum in the solid body must be conserved in each time step. To resolve an unrealistic slip condition in the solid-liquid interface, a high viscosity is attributed to the solid zone. The computation procedure applied in this paper is organized as follows:

- (1) A scalar parameter ( $\varphi_s$ ) is used to describe the solid object within the computational domain. ( $\varphi_s$ ) is defined as the fraction of total volume of a cell occupied by solid. In other words, ( $\varphi_s$ ) is the volume of solid in a cell divided by the total volume of the cell (not divided by the combined volume of liquid and gas)

$$\varphi_s = \begin{cases} 0 & \text{out of solid} \\ 0 < \varphi_s < 1 & \text{solid boundary} \\ 1 & \text{within solid} \end{cases} \quad (14)$$

- (2) The governing equations are solved everywhere even within the solid zone. The density and viscosity are calculated in each cell as follows

$$\rho = f\rho_l + (1 - f - \varphi_s)\rho_g + \varphi_s\rho_s \quad (15)$$

$$\mu = f\mu_l + (1 - f - \varphi_s)\mu_g + \varphi_s\mu_s \quad (16)$$

where liquid, gas and solid are represented by l, g, and s respectively. Based on Mirzaii and Passandideh-Fard (2012), using a viscosity two orders of magnitude larger than that of the fluid is large enough to accurately model the solid-liquid interaction.

- (3) The following integrals are used to calculate the average rotational and angular velocity based on the conservation of momentum within the solid

$$M_s \vec{V}_s = \int_{\text{solid zone}} \rho \vec{V} dV \quad (17)$$

$$I_s \vec{\omega}_s = \int_{\text{solid zone}} \vec{r} \times \rho \vec{V} dV \quad (18)$$

where the solid mass, moment of inertia, translational velocity, and angular velocity are indicated by  $M_s$ ,  $I_s$ ,  $\vec{V}_s$ ,  $\vec{\omega}_s$  respectively.  $\forall$  and  $\vec{r}$  are the solid volume and position vector with respect to the solid center of the mass. The next velocity is calculated as follows:

$$\vec{V}_{\text{solid zone}} = \vec{V}_s + \vec{\omega}_s \times \vec{r} \quad (19)$$

To eliminate the need for applying an additional force term to the solid zone, the viscosity of the solid zone is increased and so,  $\mu \rightarrow \mu^{n+1}$  is supposed to be equal with  $\vec{V}_{\text{solid zone}}$ . A flowchart of the sequence of the computational cycle for velocity, and fluid-solid volume fractions is shown in Fig. 1.

### 3. Results and discussions

Three-dimensional numerical results for water entry of a horizontal cylinder are presented in this section. To show the three-dimensional effects more clearly, the results are displayed from both the front and side views. To validate the numerical model, the results are compared with those available in the literature. Furthermore, the effects of various parameters namely solid density, initial impact velocity, length and diameter on the cylinder depth are studied. Numerical computations were performed on an Intel(R) 3.5 GHz CPU XP desktop. The computation times ranged from 5 to 8 days.

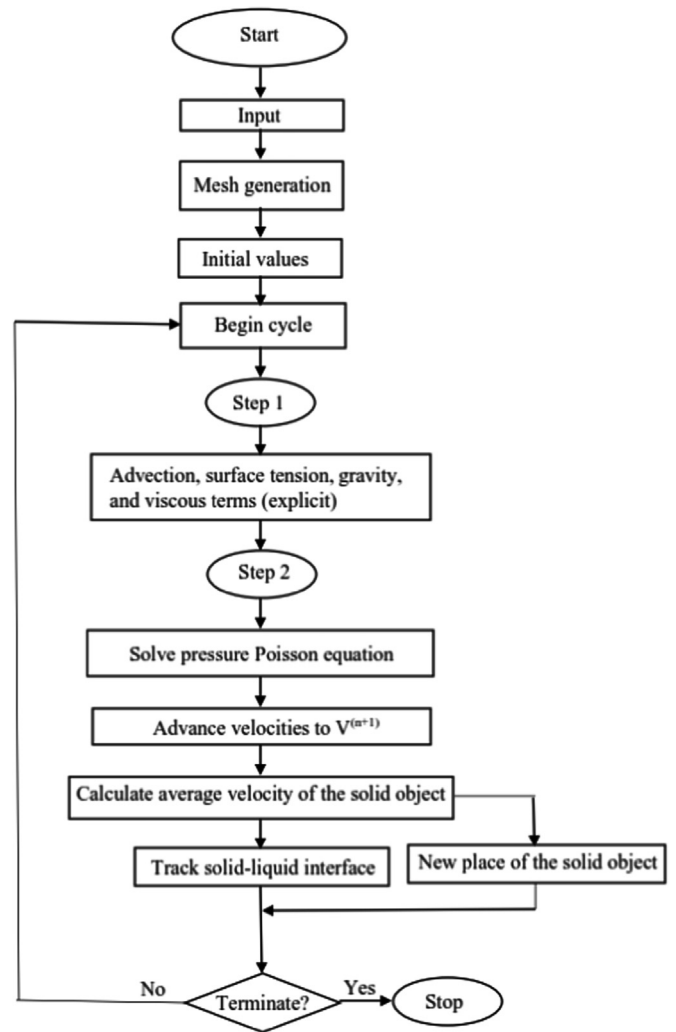


Fig. 1. Flowchart of the sequence of the computational cycle for velocity, and fluid-solid volume fractions.

#### 3.1. Water entry of a cylinder

In this section, the water entry of a horizontal cylinder is discussed both numerically and experimentally. To simulate the water entry of a cylinder, four non-dimensional parameters are required: Reynolds number  $Re=U_0d/\nu$ , Weber number  $W = \rho U_0^2 R_0/\sigma$ , Bond number  $B = \rho g R_0^2/\sigma$ , and Froude number  $Fr = U_0/\sqrt{gd}$ . Here,  $U_0$ ,  $d$ ,  $\nu$  stand for the impact velocity, cylinder diameter, and fluid kinematic viscosity ( $\nu \approx 10^{-6} \text{ m}^2/\text{s}$ ) respectively. Fluid density and surface tension, and cylinder radius are represented by  $\rho \approx 1000 \text{ kg/m}^3$ ,  $\sigma \approx 0.07 \text{ N/m}$ , and  $R_0$ . The density ratio of the solid to water is defined as  $D = \rho_{\text{solid}}/\rho_{\text{water}}$ . The experimental results used to validate the numerical model are those reported by Wei and Hu (2014) with the following specifications:

1. Cylinder length (L): 200 mm.
2. Cylinder diameter (d): 50 mm.
3. Initial position of the cylinder center: 25 mm above the water surface.
4. Impact velocity ( $U_0$ ): 6.22 m/s.
5. Solid density:  $1370 \text{ kg/m}^3$ .

The cylinder is released from a height of 2 m in the experiment (Wei and Hu, 2014); when the cylinder touches the free-surface, its impact velocity is 6.22 m/s. At this moment, the initial position of the cylinder center is 25 mm above the free-surface (since the cylinder diameter is

**Table 1**  
Values of non-dimensional parameters for the water entry experiment (Wei and Hu, 2014).

$U_0$ (m/s)	$W = \rho U_0^2 R_0 / \sigma$	$B = \rho g R_0^2 / \sigma$	$Re = U_0 d / \nu$	$Fr = U_0 / \sqrt{gd}$
6.22	$1.37 \times 10^4$	87.5	$3.09 \times 10^5$	8.89

50 mm).

The values of non-dimensional parameters used in the experiments are displayed in Table 1.

A schematic diagram of the computational domain for the water entry of a horizontal cylinder is illustrated in Fig. 2. For the simulation results presented in this manuscript, the computational domain is set sufficiently large such that no significant wall effects are observed on the cylinder velocity and depth, cavity shape, and the elevated water level on the walls. In other words, the domain is extended in all directions to make sure that the cylinder moves within the liquid region freely and the simulation results are independent of the computational domain. The same considerations have been used in the literature for water entry of solid objects (Mirzaii and Passandideh-Fard, 2012). The length, width, and height of the tank are finally assumed to be 0.80, 0.70, and 0.6 m due to the restrictions on CPU run time and computer Ram. Furthermore, water depth within the tank is 75% of the tank's height. The computational domain is solved for one-quarter of the cylinder due to its symmetry and the results are mirrored around the symmetry axes. The water is also supposed to be at rest with no movement initially.

A uniform mesh was applied to the computational domain. The mesh size can be characterized based on the cylinder length using CPL (number of cells per total length). A mesh refinement study was performed in which the grid size was gradually reduced until no significant changes were observed in the cylinder. The results of this mesh study for the cylinder depth against time is presented in Fig. 3. Based on this study, it was found that a mesh size with CPL=30 is an optimum value.

Figs. 4 and 5 show the experimental (Wei and Hu, 2014) and numerical results of a horizontal cylinder entering water. The results are presented in both 2D cross section and 3D views from the front and side views to give a better insight. Velocity profiles and streamlines are shown in the left and right sides of 2D cross section, respectively. This paper focuses more on the cavity shape formed behind the cylinder rather than the upper crown. Figs. 4 and 5 are synchronized in time to facilitate the comparison. It is supposed that at  $t_0=0$  s, the cylinder touches the water surface. Several new phenomena can be observed

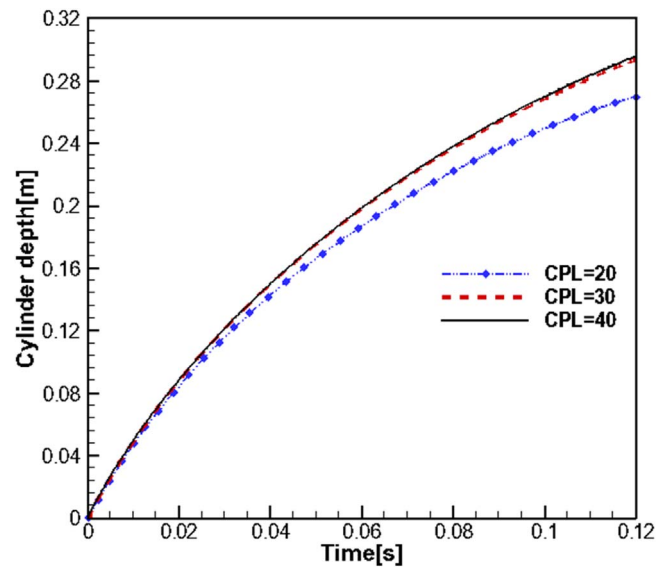


Fig. 3. The results of mesh refinement study for the depth of cylinder versus time.

from the figures. As the cylinder touches the free surface, the part of water occupied by the cylinder is ejected at the point of contact since the kinetic energy transferred to water overcomes the surface tension effects. The high-speed horizontal jetting spreads as the cylinder descends into water which is evident in experimental images. This fluid jetting cannot be observed in the side view (Fig. 5 at  $t=2$  ms). A recirculation zone is formed in the right side of the cylinder in Figs. 4 and 5 at  $t=2$  ms. This area starts to outspread and cover a wider area in Figs. 4 and 5 at  $t=4$  ms. As this region is increased, a larger volume of water is ejected at the surface contact. An open air cavity is observed behind the cylinder in Figs. 4 and 5 at  $t=12$  ms while the recirculation zone position is fixed versus time. The tails of the thin water layer move with very high speed and finally break up from the thin water layer into small drops of spray. The reduced air pressure in the cavity causes the splash to move inwards (Fig. 4 at  $t=36$  ms). At the same time, an approximately vertical curtain called splash crown is formed as a result of the splash growing upward. This phenomenon is partly captured by the numerical results (Figs. 4 and 5 at  $t=36$  ms). As the cylinder descends completely into water, the flow is separated from the cylinder surface in both side and right directions (Figs. 4 and 5 at  $t=36$  ms). Based on Fig. 4 at  $t=12-74$  ms, the two pairs of cross lines at each end of the cylinder move faster than other parts of the cavity and begin

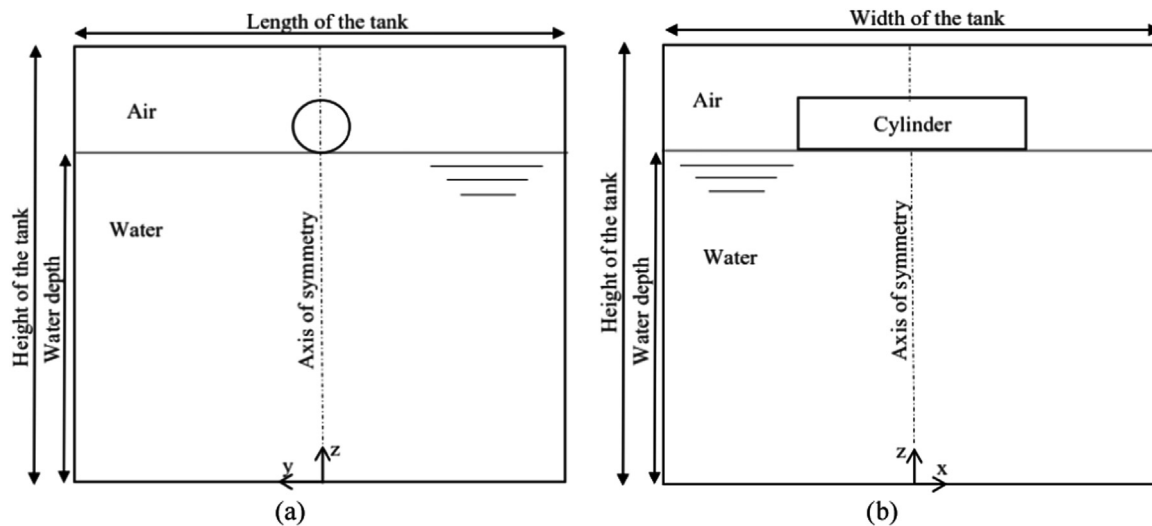
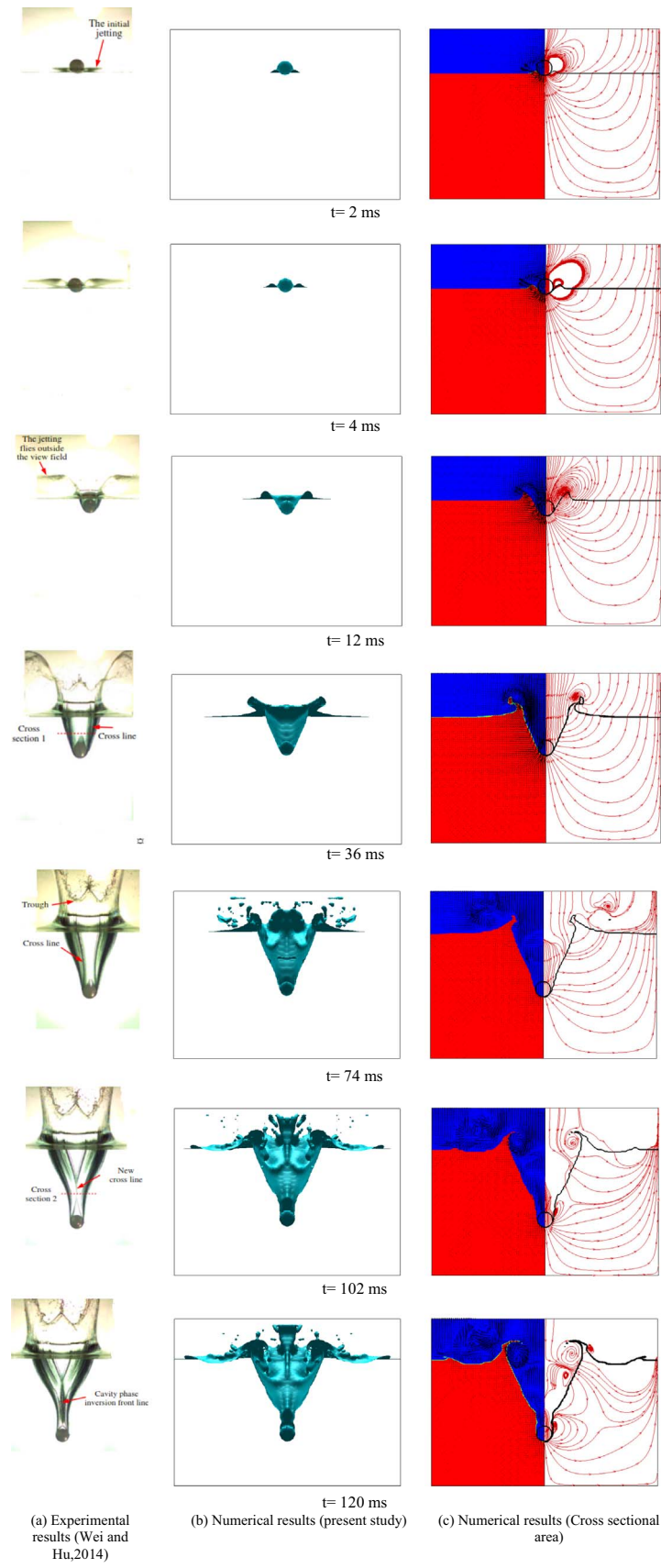
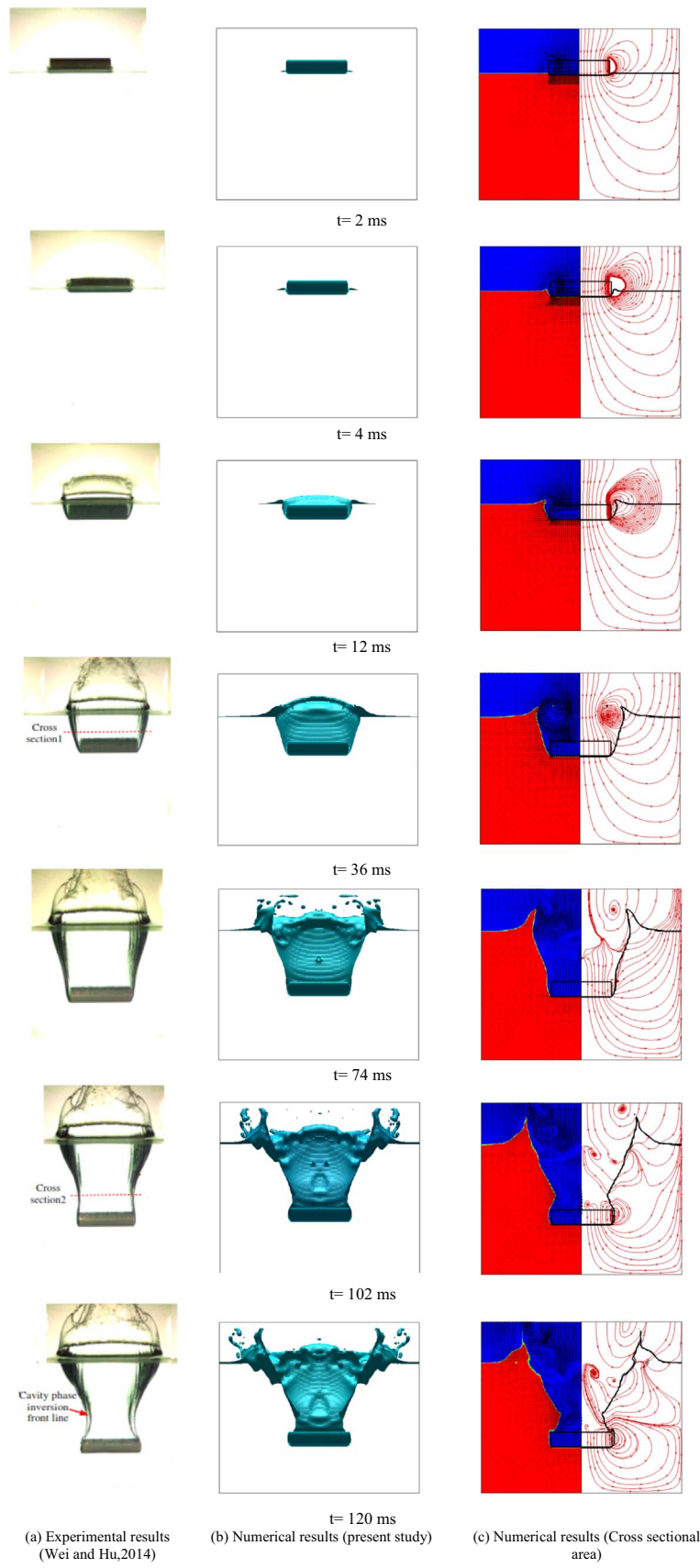


Fig. 2. Schematic diagram of a horizontal cylinder during its water entry (a) Front view (b) Side view.



**Fig. 4.** Experimental and numerical results of a horizontal circular cylinder entering water (front view).



**Fig. 5.** Experimental and numerical results of a horizontal circular cylinder entering water (side view).

approaching each other. In Figs. 4 and 5 at  $t=102$  ms, further recirculation zones are generated both inside and outside the cavity and also the direction of streamlines are entirely changed. The recirculation zone formed in front of the cylinder causes the cavity walls approaching each other (Fig. 4 at  $t=102$  ms). After the two pairs of cross lines close, two new cross lines are generated (Fig. 4 at  $t=102$  ms). They also move along the axis direction faster than other parts of the cavity (Figs. 4 and 5 at  $t=102$ – $120$  ms). In Fig. 4 at  $t=120$  ms, the directions of streamlines are completely reversed. The recirculation zone covers the entire right side of the cylinder in Fig. 5 at  $t=120$  ms. As shown in Fig. 5, the side wall of the cavity from the experiments is smooth while there are some elevated streaks on the cavity wall from simulations. The small discrepancy between the calculated images and experimental photos related to the cavity wall may be attributed to the small roughness of the cylinder surface along with its corresponding contact angle variations in the experiments. Furthermore, the cavity shape inversion behavior cannot be seen in the numerical results. The cavity shape inversion line is attributed to the reattachment of thin liquid films separated from the two ends of the cavity. Modeling thin liquid films needs extensive mesh refinements which will considerably increase the computational time. The flow separation from the cylinder surface may be attributed to the surface conditions (small roughness and contact angle variations) which was not the focus of this manuscript.

The experimental (Wei and Hu, 2014) and numerical results are well compared qualitatively. To present a quantitative comparison, the cylinder depth versus time are plotted in Fig. 6. As observed, the results of simulation agree well with those of the experiment. For early times, the small differences between the experimental and numerical results can be attributed to the assumptions used in numerical simulations. In the developed model, the surface of the cylinder is assumed to be smooth and hydrophobic. This means that no specific treatment is used for the contact angle between the solid and liquid. The free surface in sharp edges tends to form a curvature because of the surface tension effects. This effect completely mimics the cases in which a hydrophobic solid enters a liquid free surface (Mirzaei and Passandideh-Fard, 2012).

It should also be noted that errors in the measurement of impact velocity in experiments have been reported in the literature. Wei and Hu (2014) reported that the initial jetting speed error is estimated to be within 10%. Quantitative comparison between the experimental (Wei and Hu, 2014) and numerical depths of a horizontal circular cylinder entering water is presented in Table 2. As seen in this table, the

**Table 2**

Comparison between the experimental (Wei and Hu, 2014) and numerical (present study) depths of a horizontal cylinder entering water.

Time (ms)	20	40	60	80	100	120
Numerical depth (m)	0.0881	0.1499	0.1984	0.2378	0.2698	0.2956
Experimental depth (m)	0.0910	0.1576	0.2121	0.2542	0.2895	0.3177
Absolute error (m)	0.0029	0.0077	0.0137	0.0164	0.0197	0.0221
Relative error (%)	3.1868	4.8858	6.4592	6.4516	6.8048	6.9562

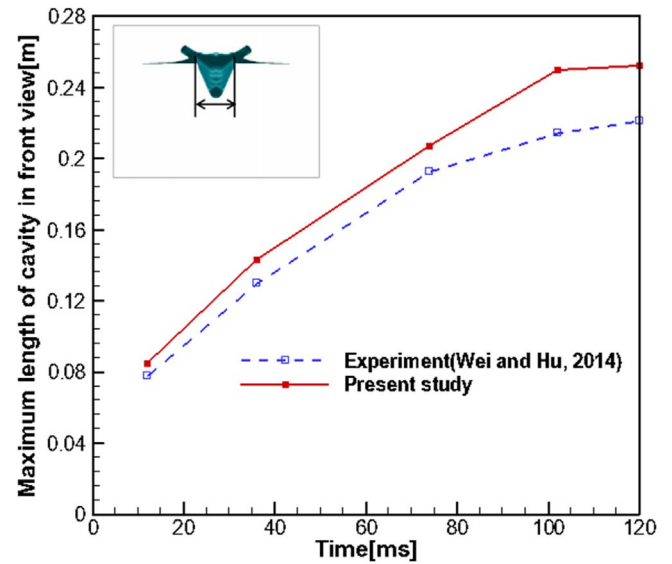


Fig. 7. Comparison between maximum length of cavity (front view) formed in experimental and numerical results.

absolute errors between the above-mentioned depths are increased over time, while the relative errors vary between 3% and 7% for the selected times in Table 2.

Maximum length of the cavity formed in experimental and numerical results are measured and compared with each other in Figs. 7 and 8 from both front and side views, respectively. Based on Figs. 7 and 8, the difference between the cavity length in numerical and experimental results is small from front and side views until  $t=75$  ms. This difference

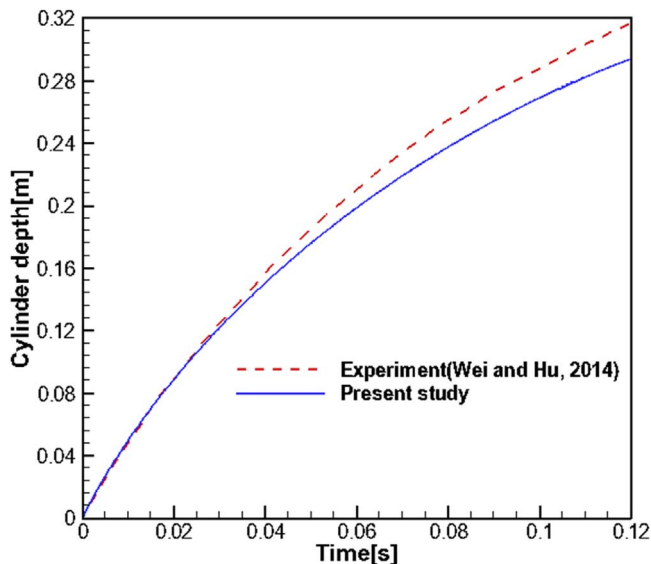


Fig. 6. Comparison between the experimental and theoretical depth versus time for water entry of a horizontal cylinder.

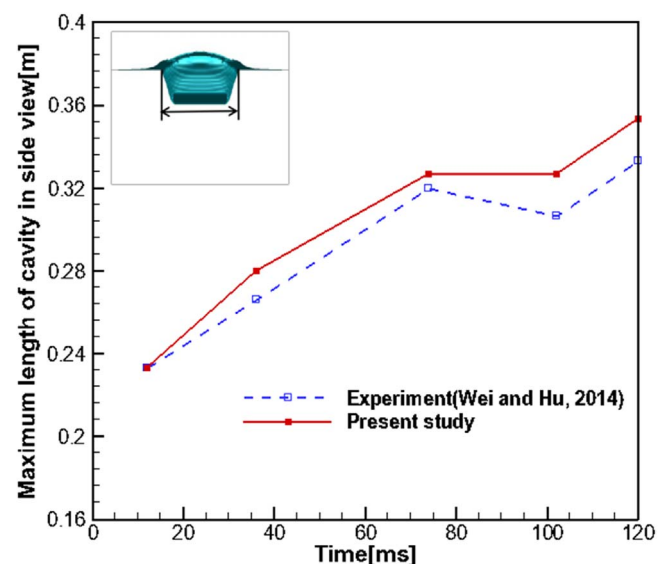


Fig. 8. Comparison between maximum length of cavity (side view) formed in experimental and numerical results.

is increased after  $t=75$  ms. Moreover, maximum lengths of the cavity in the front and side views are more than those in the experiment for all times.

### 3.2. Considering the effects of various parameters on the cylinder trajectory

In this section, the effects of various parameters namely length, diameter and density of the cylinder and also the cylinder impact velocity on its motion are studied. To investigate the effects of three-dimensional effects more clearly, five lengths (0.05, 0.1, 0.2, 0.3, 0.4 m), three diameters (0.05, 0.075, 0.1 m), three density ratios (0.9, 1.15, 1.37) and three impact velocities (6.22, 5.2, 4.37 m/s) are considered. As the cylinder descends into water, the end effects will influence the resulting force and finally affects the cylinder depth. Two non-dimensional parameters namely non-dimensional depth ( $h^*$ ) and non-dimensional time ( $t^*$ ) are defined to evaluate these effects more precisely. These parameters are defined as follows:

$$h^* = \frac{h}{d} \tag{20}$$

$$t^* = \frac{t \times V_s}{d} \tag{21}$$

where  $h$ ,  $V_s$ ,  $t$  are the cylinder depth, cylinder average velocity, and time, respectively.

To better study the effect of each parameter, only one parameter is varied at a time while the other parameters are kept constant. Based on Figs. 9–12, the cylinder impact velocity and cylinder-water density ratio have the lowest and highest effects on the cylinder non-dimensional depth, respectively. The effects of cylinder diameter and length on its motion are approximately the same. It is also observed that the cylinder with  $L=0.4$  m has the highest deceleration while the cylinder with  $L=0.05$  m has the lowest deceleration. It is also found that the cylinder length slightly affects its non-dimensional depth in the liquid. Based on Fig. 11, three-dimensional effects become less important for cylinder lengths larger than  $L=0.2$  m.

### 4. Conclusion

A 3D numerical scheme was developed in this paper to simulate the hydrodynamics of a circular cylinder entering water horizontally. The

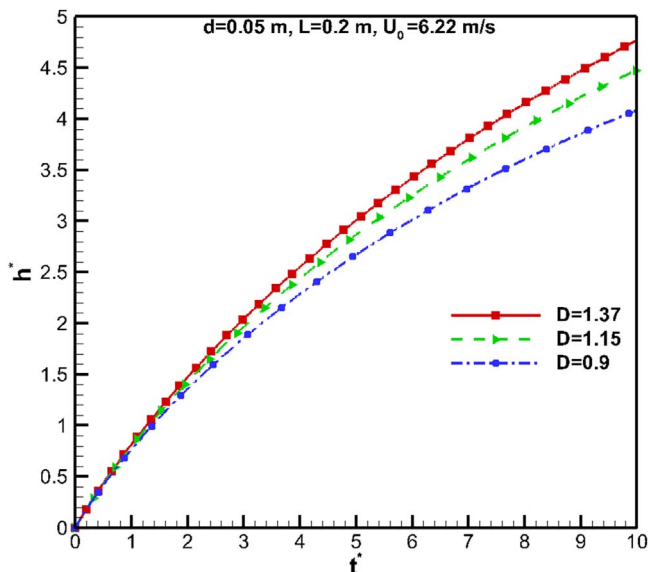


Fig. 9. The non-dimensional depth of a horizontal circular cylinder with  $d=0.05$  m,  $L=0.2$  m, and  $U_0=6.22$  m/s versus non-dimensional time for various cylinder-water density ratios ( $D$ ).

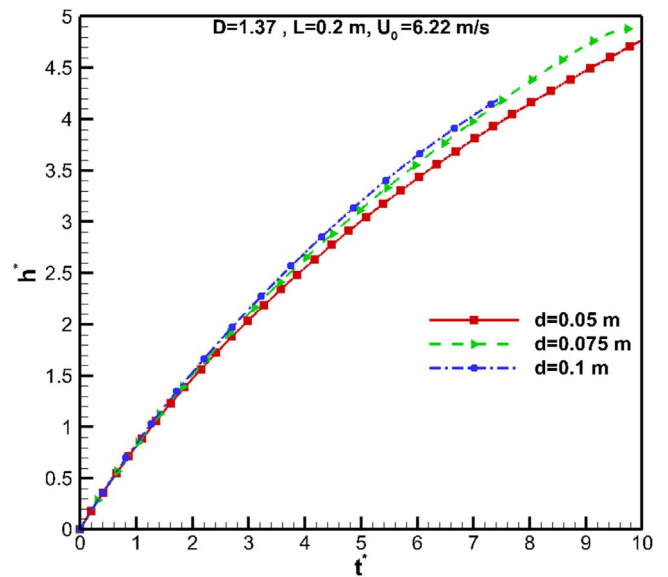


Fig. 10. The non-dimensional depth of a horizontal circular cylinder with  $D=1.37$ ,  $L=0.2$  m, and  $U_0=6.22$  m/s versus non-dimensional time for various cylinder diameters.

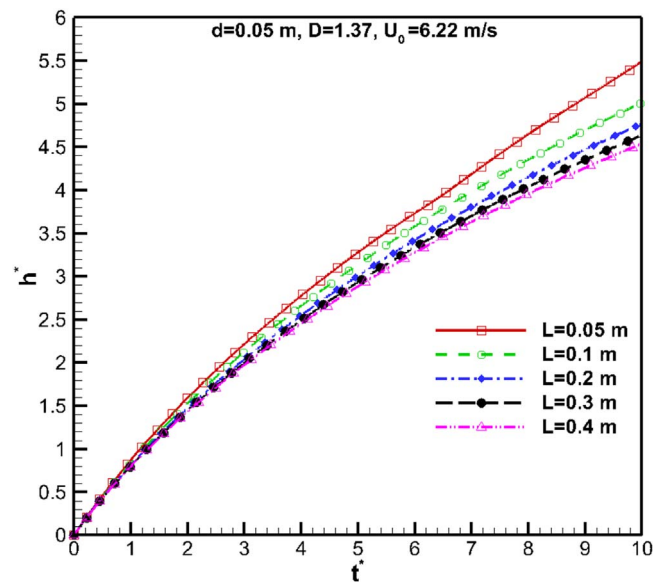


Fig. 11. The non-dimensional depth of a horizontal circular cylinder with  $d=0.05$  m,  $D=1.37$ , and  $U_0=6.22$  m/s versus non-dimensional time for various cylinder lengths.

solid-liquid interaction in presence of a free-surface was modelled by applying the governing equations namely continuity and Navier-Stokes equations along with an equation to track the free-surface (VOF method). At the first step, the governing equations were applied everywhere including the solid zone. Then, the solid body motion was applied to the region occupied by the cylinder. The viscosity of the region occupied by the cylinder was also increased to satisfy the no-slip boundary condition implicitly. The numerical results were compared with those of the experiments available in the literature to validate the numerical approach quantitatively and qualitatively. The numerical results were in a good agreement with the experimental data. Furthermore, the effects of different parameters namely diameter, length, density ratio, and cylinder impact velocity on the non-dimensional depth were investigated. The following conclusions were made:

1. Cylinder-water density ratio had a great effect on the cylinder non-dimensional depth in comparison with the cylinder impact velocity

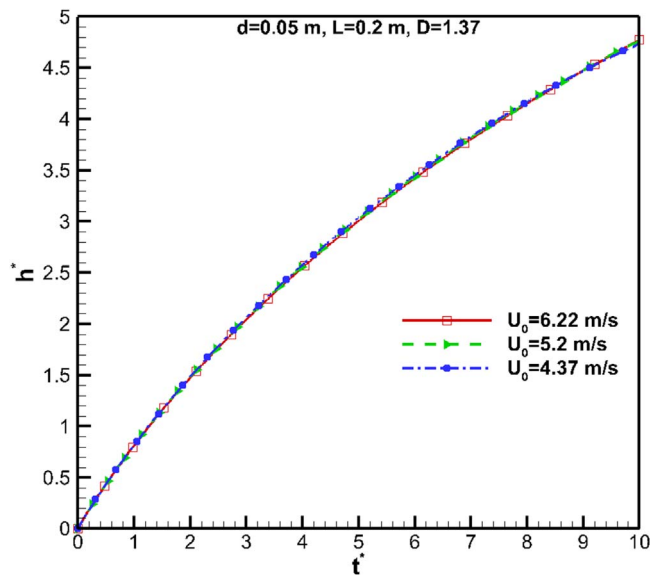


Fig. 12. The non-dimensional depth of a horizontal circular cylinder with  $d=0.05$  m,  $L=0.2$  m, and  $D=1.37$  versus non-dimensional time for various cylinder impact velocities.

for all times.

- The cylinder with the largest length experienced the highest deceleration.
- The length effect was minor at the start time of the cylinder submerge and as the time passed, this effect became more important.
- Three-dimensional effects became less significant for cylinder lengths larger than 0.2 m.
- Maximum lengths of the cavity in the front and side view were more than those in the experiment for all times. Furthermore, the difference between the cavity length in numerical and experimental results was small for front and side views until  $t=75$  ms. This difference increased after  $t=75$  ms.
- While the absolute difference between the measured and calculated cylinder depths were increased in time, the relative errors varied between 3% and 7%.

## Acknowledgements

The authors would like to acknowledge the high-performance computing (HPC) center of the Ferdowsi University of Mashhad.

## References

Abelson, H.I., 1970. Pressure measurements in the water-entry cavity. *J. Fluid Mech.* 44, 129–144.

Abraham, J., Gorman, J., Reseghetti, F., Sparrow, E., Stark, J., Shepard, T., 2014. Modeling and numerical simulation of the forces acting on a sphere during early-water entry. *Ocean Eng.* 76, 1–9.

Aleinov, I., Puckett, E.G., 1995. Computing surface tension with high-order kernels. In: *Proceedings of the Sixth International Symposium on Computational Fluid Dynamics*, Lake Tahoe, NV, pp. 13–18.

Aristoff, J.M., Bush, J.W.M., 2009. Water entry of small hydrophobic spheres. *J. Fluid Mech.* 619, 45–78.

Aristoff, J.M., Truscott, T.T., Techet, A.H., Bush, J.W.M., 2010. The water entry of decelerating spheres. *Phys. Fluids* 22, 8.

Brackbill, J.U., Kothe, D.B., Zemach, C., 1992. A continuum method for modeling surface tension. *J. Comput. Phys.* 100, 335–354.

Challa, R., Yim, S.C., Idichandy, V.G., Vendhan, C.P., 2014. Rigid-object water-entry impact dynamics: Finite-element/smoothed particle hydrodynamics modeling and experimental validation. *J. Offshore Mech. Arct. Eng.* 136, 031102–031112.

Erfanian, M.R., Anbarsooz, M., Rahimi, N., Zare, M., Moghiman, M., 2015. Numerical and experimental investigation of a three dimensional spherical-nose projectile water entry problem. *Ocean Eng.* 104, 397–404.

Gilberg, D., Andersok, R.A., 1948. Influence of atmospheric pressure on the phenomena accompanying the entry of spheres into water. *J. Appl. Phys.* 19, 127.

Glowinski, R., 2003. *Numerical Methods for Fluids (Part 3)*. Elsevier Science B.V., Amsterdam, The Netherlands.

Glowinski, R., Pana, T.W., Hesla, T.I., Joseph, D.D., 1999. A distributed Lagrange multiplier/fictitious domain method for particulate flows. *Int. J. Multiphas. Flow* 25, 755–794.

Glowinski, R., Pan, T.W., Hesla, T.I., Joseph, D.D., Periaux, J., 2001. A fictitious domain approach to the direct numerical simulation of incompressible viscous flow past moving rigid bodies: application to particulate flow. *J. Comput. Phys.* 169, 363–426.

Goharzadeh, A., Molki, A., 2012. Experimental study of water entry and exit of a circular cylinder at free surface. In: *Proceedings of the ASME 2012 International Mechanical Engineering Congress and Exposition, IMECE2012*, Texas, USA.

Greenhow, M., Lin, W.M., 1983. *Nonlinear Free Surface Effects: Experiment and Theory*. Rep. 83-19. Department of Ocean Engineering, MIT.

Gu, H.B., Qian, L., Causon, D.M., Mingham, C.G., Lin, P., 2014. Numerical simulation of water impact of solid bodies with vertical and oblique entries. *Ocean Eng.* 75, 128–137.

Hafsia, Z., Mnasri, C., Mohamed, O., Maalel, K., 2009. Water entry and exit of horizontal cylinder in free surface flow. In: *Proceedings of the International Symposium on Convective Heat and Mass Transfer in Sustainable Energy*, Tunisia, April 26.

Hu, C., Koterayama, W., 1996. Slow drift damping force acting on a horizontal cylinder. *J. Mar. Sci. Technol.* 1, 105–113.

Hu, C., Sueyoshi, M., 2010. Numerical simulation and experiment on dam break problem. *J. Mar. Sci. Appl.* 9, 109–114.

Kershaw, D.S., 1978. The incomplete Cholesky–conjugate gradient method for the iterative solution of systems of linear equations. *J. Comput. Phys.* 26, 43–65.

Landau, L.D., Lifschitz, E.M., 1987. *Fluid Mechanics* second ed. Pergamon Press, Oxford.

Larsen, E., 2013. Impact loads on circular cylinders. *Inst. Mar. Tek.*

Lee, M., Longoria, R.G., Wilson, D.E., 1997. Cavity dynamics in high-speed water entry. *Phys. Fluids* 9, 540.

Lin, P., 2007. A fixed-grid model for simulation of a moving body in free surface flows. *Comput. Fluids* 36, 549–561.

Lue, H., Wang, H., Soares, C.G., 2012. Numerical and experimental study of hydrodynamic impact and elastic response of one free-drop wedge with stiffened panels. *Ocean Eng.* 40, 1–14.

May, A., 1951. Effect of surface condition of a sphere on its water entry cavity. *J. Appl. Phys.* 22, 4.

May, A., 1952. Vertical entry of missiles into water. *J. Appl. Phys.* 23, 1362–1372.

Mirzaei, I., Passandideh-Fard, M., 2012. Modeling free surface flows in presence of an arbitrary moving object. *Int. J. Multiphas. Flow* 39, 216–226.

Moghisi, M., Squire, P.T., 1981. An experimental investigation of the initial force of impact on a sphere striking a liquid surface. *J. Fluid Mech.* 108, 133–146.

Nuffel, D.V., Vepa, K.S., Baere, I.D., Lava, P., Kersemans, M., Degrieck, J., Rouck, J.D., Paepegem, W.V., 2014. A comparison between the experimental and theoretical impact pressures acting on a horizontal quasi-rigid cylinder during vertical water entry. *Ocean Eng.* 77, 42–54.

Panciroli, R., Shams, A., Porfiri, M., 2015. Experiments on the water entry of curved wedges: high speed imaging and particle image velocimetry. *Ocean Eng.* 94, 213–222.

Passandideh-Fard, M., Chandra, S., Mostaghimi, J., 2002. A three dimensional model of droplet impact and solidification. *Int. J. Heat. Mass Transf.* 45, 2229–2242.

Patankar, N.A., 2001. A formulation for fast computations of rigid particulate flows. *Cent. Turbul. Res. Evanst.*, 12.

Patankar, N.A., Sharma, N., 2005. A fast projection scheme for the direct numerical simulation of rigid particulate flows. *Commun. Numer. Methods Eng.* 21, 419–432.

Ryzhakov, P., Rossi, R., Vina, A., Onate, E., 2013. Modelling and simulation of the sea-landing of aerial vehicles using the Particle Finite Element Method. *Ocean Eng.* 66, 92–100.

Techet, A.H., Truscott, T.T., 2011. Water entry of spinning hydrophobic and hydrophilic spheres. *J. Fluids Struct.* 27, 716–726.

Thoroddsen, S.T., Etoh, T.G., Takehara, K., Takano, Y., 2004. Impact jetting by a solid sphere. *J. Fluid Mech.* 499, 139–148.

Wagner, H., 1932. Über Stoß- und Gleitvorgänge an der Oberfläche von Flüssigkeiten. *ZAMM. J. Appl. Math. Mech./Z. Angew. Math. Mech.* 12 (4), 193–215.

Wang, S., Soares, C.G., 2014. Numerical study on the water impact of 3D bodies by an explicit finite element method. *Ocean Eng.* 78, 73–88.

Watanabe, S., 1934. Resistance of impact on water surface. Part V—sphere. *Sci. Pap. Inst. Phys. Chem. Res.* 484, 202–208.

Wei, Z., Hu, C., 2014. An experimental study on water entry of horizontal cylinders. *J. Mar. Sci. Technol.* 19, 338–350.

Wei, Z., Hu, C., 2015. Experimental study on water entry of circular cylinders with inclined angles. *J. Mar. Sci. Technol.* 20, 722–738.

Wen, P., Qiu, W., 2016. Solving 2D water entry problems with a CIP method and a parallel computing algorithm. *Mar. Syst. Ocean Technol.* 11, 1–9.

Worthington, A.M., 1908. *A Study of Splashes*. Longmans, Green, and Co., London.

Worthington, A.M., Cole, R.S., 1897. Impact with a liquid studied by the aid of instantaneous photography. *Philos. Trans. R. Soc. A (Contain. Math. Phys. Character)* 189, 137–1480.

Yang, Q., Qiu, W., 2012a. Numerical simulation of water impact for 2D and 3D bodies. *Ocean Eng.* 43, 82–89.

Yang, Q., Qiu, W., 2012b. Numerical solution of 3D water entry problems With a constrained interpolation profile method. *J. Offshore Mech. Arct. Eng.*, 134.

Youngs, D.L., 1984. *An Interface Tracking Method for a 3D Eulerian Hydrodynamics Code*. Technical Report 44/92/35, AWRE.

Zhu, X., Faltinsen, O.M., Hu, C., 2006. Water entry and exit of a horizontal circular cylinder. *J. Offshore Mech. Arct. Eng.* 129, 253–264.